Tairan Fu[1]
Key Laboratory for Thermal Science and Power Engineering of Ministry of Education, Beijing Key Laboratory of CO_2 Utilization and Reduction Technology, Department of Energy and Power Engineering, Tsinghua University, Beijing 100084, China
e-mail: trfu@mail.tsinghua.edu.cn

Jiangfan Liu
Key Laboratory for Thermal Science and Power Engineering of Ministry of Education, Beijing Key Laboratory of CO_2 Utilization and Reduction Technology, Department of Energy and Power Engineering, Tsinghua University, Beijing 100084, China

Minghao Duan
Key Laboratory for Thermal Science and Power Engineering of Ministry of Education, Beijing Key Laboratory of CO_2 Utilization and Reduction Technology, Department of Energy and Power Engineering, Tsinghua University, Beijing 100084, China

Sen Li
State Key Laboratory of High Temperature Gas Dynamics, Institute of Mechanics, Chinese Academy of Sciences, Beijing 100190, China

Subpixel Temperature Measurements in Plasma Jet Environments Using High-Speed Multispectral Pyrometry

A high-speed (2 kHz) near-infrared (1.0–1.65 μm) multispectral pyrometer was used for noninvasive measurements of the subpixel temperature distribution near the sharp leading edge of a wing exposed to a supersonic plasma jet. The multispectral pyrometer operating in the field measurement mode was able to measure the spatial temperature distribution. Multiple spectra were used to determine the temperature distributions in the measurement region. The spatial resolution of the multispectral pyrometer was not restricted to one "pixel" but was extended to subpixel accuracy (the temperature distribution inside one pixel in the image space corresponding to the point region in the object space). Thus, this system gives high-speed, multichannel, and long working time spatial temperature measurements with a small data stream from high-speed multispectral pyrometers. The temperature distribution of the leading edge of a ceramic wing was investigated with the leading edge exposed to extreme convective heating from a high-enthalpy plasma flow. Simultaneous measurements with a multispectral pyrometer and an imaging pyrometer verify the measurement accuracy of the subpixel temperature distribution. Thus, this multispectral pyrometry can provide in situ noninvasive temperature diagnostics in supersonic plasma jet environments. [DOI: 10.1115/1.4038874]

Keywords: temperature, multispectral, pyrometer, optical diagnostics, plasma

1 Introduction

Plasma wind tunnel testing of high temperature components in extreme supersonic environments is important for designing high-performance vehicles. Ultra-high temperature materials are needed for the sharp wing edges or other components on high-speed vehicles. Sharp leading edges with curvature radii on the order of a few millimeters are used to reduce the aerodynamic drag and improve the maneuverability. The sharp configuration of the leading edge can lead to surface temperatures at the stagnation point exceeding 1000 °C due to the extreme hypersonic aerodynamic heating [1–5]. Therefore, designs are needed to ensure the structural integrity of the sharp leading edges in such harsh aerodynamic environments. The development of these supersonic wing designs then requires fast, noninvasive in situ measurements of the temperature distribution along the sharp leading edges in aerodynamic ground-based experiments.

Optical pyrometer techniques can be used for noninvasive, high-temperature applications. There are various optical imaging techniques that have been developed based on visible, near-infrared, and infrared focal plane image sensors to measure the temperatures distribution of hot surfaces [6–13] and combustion processes [14–20]. For example, Simmons et al. [8] measured the temperatures of two large thermionic tungsten cathodes by a combination of multispectral imaging using a conventional charge coupled device (CCD) camera and three spot pyrometers. Densmore et al. [17] calibrated a digital high-speed color camera to measure the temperatures of explosive and combustion processes. A two-color ratio method was used to calculate the temperature using a color-filtered raw image data and the graybody assumption. Optical thermography can measure two-dimensional (2D), surface temperature distributions with excellent spatial resolution. The imaging pyrometer generally needs to have a high frequency, high resolution sensor for long tests with fast transients in aerodynamic environments. These requirements result in huge data streams for two-dimensional, transient temperature measurements, which is a shortcoming for in situ measurements. In addition, the limited number of spectrum channels for the imaging measurements due to the instrumentation limits the temperature accuracy.

Conventional optical imaging pyrometers measure the radiation spectrum over a single waveband with a two-dimensional array of pixels. Multispectral pyrometers are generally point measurement systems that measure the spectra at one point so they have excellent hyperspectral resolution without the spatial resolution of imaging pyrometers. Multispectral pyrometry is a well-established method to measure the temperatures of combustion flames or hot surfaces from spectral intensity measurements using multiple spectra with an assumed emissivity function [21–37]. Tapetado et al. [21,22] proposed a fiber-optic two-color pyrometer using glass multimode fibers with 62.5 μm diameters and a 0.275 numerical aperture to measure the temperature evolution of a Inconel 718 workpiece and machined surfaces for different cutting conditions. Ng and Fralick [23] used a multiwavelength pyrometer

[1]Corresponding author.

Contributed by the Heat Transfer Division of ASME for publication in the JOURNAL OF HEAT TRANSFER. Manuscript received March 7, 2017; final manuscript received October 22, 2017; published online April 6, 2018. Assoc. Editor: Thomas Beechem.

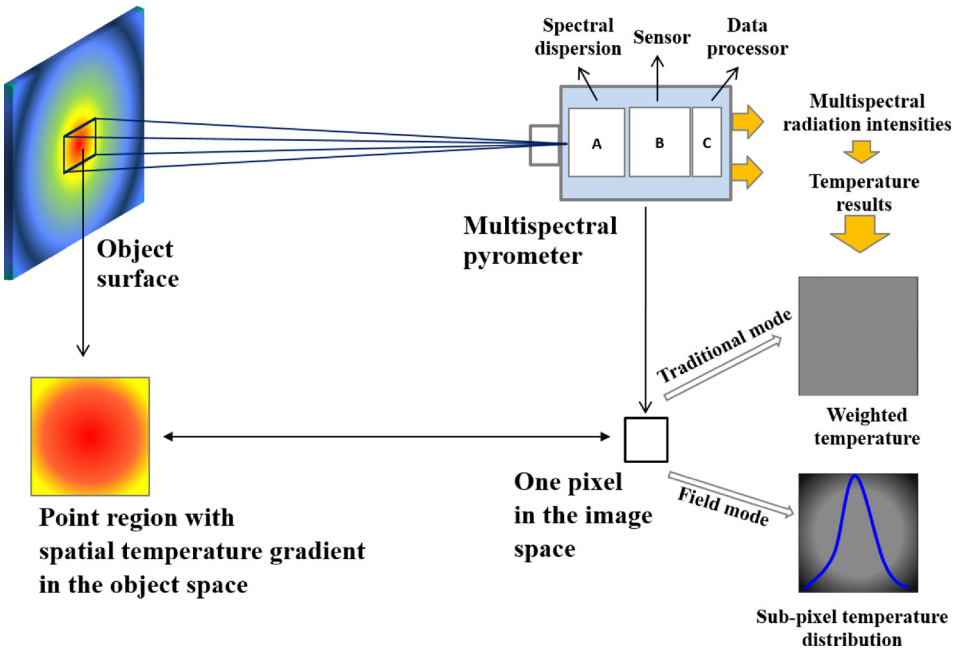

Fig. 1 Temperature measurement modes of a multispectral pyrometer

for temperature measurements of thermal barrier coatings, glass materials, and combustor gases. Wen and Mudawar [25] experimentally assessed the accuracy of multispectral radiation thermometry emissivity models for temperature measurements. Duvaut [29] reviewed the theoretical development and research status of multiwavelength pyrometry and compared experimental results obtained in the visible and middle infrared spectral ranges. Fu et al. [31–35] developed a multispectral pyrometer for the visible and near-infrared spectral ranges for temperature measurements of combustion flames, nontransparent surfaces, and semitransparent materials.

The large amounts of spectral data from multispectral pyrometers significantly reduce the measurement uncertainty. Point multispectral pyrometers are fast, have multiple channels, can record for long times, and have small data streams. However, most multispectral pyrometers only measure the temperature at one point or in a spatially averaged region. Thus, these are zero-dimensional measurements in terms of the spatial resolution so they cannot measure surface temperature profiles on objects with high spatial temperature gradients such as the leading edges of wings. Therefore, there is a need for temperature measurements in aerodynamic environments using advanced optical pyrometers. This work introduces a high speed, multispectral pyrometer for fast, in situ, noninvasive measurements of subpixel temperature distributions along the sharp leading edges of wings in supersonic plasma jet environments.

2 Method

The optical-electronic sensor of a multispectral pyrometer measures the thermal radiation energy from a point or from a spatially averaged region. Thus, one sensor pixel represents the thermal radiation energy from a point or spatially averaged region. Multiple sensor pixels in a multispectral pyrometer then correspond to multiple spectra at the same point or spatially averaged region in the traditional working mode, called the point measurement mode, of a multispectral pyrometer. The pyrometer field of view is then only a point region without geometrical dimensions with the measured "point" temperature in the traditional measurement mode being the weighted temperature of the point region. Multispectral pyrometers cannot measure the temperature distribution inside the pixel corresponding to the point region, so the pyrometers cannot measure spatial temperature gradients. Although the point region size may be reduced to reduce the effects of the spatially nonuniform temperatures within the point region, multispectral pyrometers cannot measure temperature gradients in the traditional mode.

The multispectral pyrometer described in this paper uses a two-dimensional field measurement mode. The multiple spectra data in the point region can then be used to determine the subpixel temperature distribution inside one pixel corresponding to the point region. A multispectral pyrometer operating in the field measurement mode can measure spatial temperature distributions. The spatial temperature distribution information then depends on the multispectral information of the point region instead of the method used by traditional two-dimensional image sensors. The multispectral pyrometer setup is shown in Fig. 1.

For an isothermal point region, the measured spectral radiation intensity, $I_{\lambda_i,\text{meas}}$, at wavelength λ_i measured by a multispectral pyrometer in the traditional measurement mode [31,32] is

$$I_{\lambda_i,\text{meas}} = \varepsilon(\lambda_i, T) I_b(\lambda_i, T), \quad i = 1 \ldots N \tag{1}$$

where T is the temperature, ε is the spectral emissivity, I_b is the spectral radiation intensity distribution of a blackbody at the same temperature, i is the index of the wavelength channel, and N is the number of channels in the multispectral pyrometer. The spectral range of the pyrometer with N measurement wavelengths is divided into multiple spectral subregions [31,32]. The emissivity in each spectral subregion, j, can then be characterized by simple functions (for example, a linear or exponential function). The least squares method or other optimization algorithms can then be used to solve for the temperature and spectral emissivity by minimizing the function,

$$F = \sum_{i=1}^{N} \left(I_{\lambda_i,\text{meas}} - \varepsilon_j(\lambda_i) I_{\lambda_i,b}\right)^2 \tag{2}$$

For the field measurement mode, the temperature range in a point region with a spatial temperature gradient is divided into M discrete temperatures, $(T_1, T_2, \ldots, T_M)$, with the same temperature interval $\Delta T = T_{j+1} - T_j$. The measured radiation intensity, $I_{\lambda,\text{meas}}$,

emitted from this nonisothermal region and received by a pyrometer is given by the sum of the intensities over the temperature range

$$I_{\lambda_i,\text{meas}} = \sum_{j=1}^{M} \varepsilon I_b(\lambda_i, T_j) r(T_j), \quad i = 1 \ldots N \tag{3}$$

where ε is assumed to be a constant or a known function of the temperature. This analysis assumes that the gray surface emissivity does not vary with the temperature to simplify the analysis, as is often assumed for temperature ranges of less than 400 °C. $r(T_j)$ is the temperature area fraction function which is the ratio of the area with a temperature range of $(T_j - \Delta T/2, T_j + \Delta T/2)$ to the total area of the point region. The condition of $\sum_{j=1}^{M} r(T_j) = 1$ is also satisfied. The average temperature, T_{ave}, in the point region can be expressed using $r(T)$ as

$$T_{\text{ave}} = \sum_{j=1}^{M} T_j r(T_j) \tag{4}$$

Equation (3) is the basic equation for the field measurement mode for multispectral pyrometers. $r(T) = 1$ for an isothermal point region which then gives Eq. (1). The temperature area fraction function, $r(T)$, is a dimensionless quantity that describes the area distribution for different temperatures in the point region that reflects the subpixel temperature distribution information inside one pixel in the image space corresponding to the point region in the object space.

Equation (3) can be rewritten in matrix form as

$$\mathbf{E} \cdot \mathbf{X} = \mathbf{L} \tag{5}$$

where $\mathbf{E}$ is an $N \times M$ matrix with $E_{i,j} = I_b(\lambda_i, T_j)$, $i = 1, \ldots, N$, $j = 1, \ldots, M$. $\mathbf{X}$ is an M column vector of the solutions, $\mathbf{X} = (\varepsilon r(T_1), \ldots, \varepsilon r(T_M))$. $\mathbf{L}$ is an N column vector of the measured spectral radiation intensities, $\mathbf{L} = (I_{\lambda_1,\text{meas}}, \ldots, I_{\lambda_i,\text{meas}}, \ldots, I_{\lambda_N,\text{meas}})$. When $N \geq M$, the temperature area fraction function, $(r(T_1), \ldots, r(T_M))$, can be found from the measured multiple spectral radiation intensities using an inversion algorithm.

This study used the improved Levenberg–Marquardt algorithm with a penalty function and an intensity weighting correction to solve this ill-posed inverse problem [35]. Then, the function $F_{i,v}$ based on Eq. (5)

$$F_{i,v} = I_{\lambda_i,\text{meas}} \Big/ \sum_{j=1}^{M} \varepsilon [I_b(\lambda_i, T_j) r(T_j) + v([\min(r(T_j), 0)]^2 + [\min(1 - r(T_j), 0)]^2)] - 1, \quad i = 1 \ldots N \tag{6}$$

where ν is the penalty parameter with $\nu > 0$ [38]. The iterative solutions, $(r(T_1), \ldots, r(T_M))$, can be determined by minimizing

$$F_v = \sum_{i=1}^{N} F_{i,v}^2 \tag{7}$$

Actual measurements must consider the random measurement noise of the measured spectral radiation intensities. The accuracy of the ill-posed inverse problem is normally improved using multiple calculations for a range of random noise levels with a normal distribution using the Levenberg–Marquardt algorithm with the average of the multiple results used as the solution.

Thus, multispectral pyrometry using the field measurement mode can be used to measure the spatial temperature distribution within a nonisothermal region from the multiple spectra. The spatial resolution of a point multispectral pyrometer is not restricted to just one "pixel" corresponding to the point region, but can be expanded to a subpixel temperature distribution in the point region with fast, long-term spatial temperature distribution measurements with small data streams. This method is very useful for fast, in situ, noninvasive temperature distribution measurements on the sharp leading edges of wings inside supersonic plasma jet environments.

3 Experiments

A high-speed multispectral pyrometer [31–33] with a near-infrared response (1.0–1.65 μm) and a maximum measurement frequency of 2 kHz was used to measure the temperature distributions in the plasma jet environments. The near-infrared spectra are more sensitive than far-infrared spectra high-temperature measurements and reduce the uncertainty due to the emissivity. Also, the near-infrared spectra reduce the interference by the radiation emitted by the nonequilibrium supersonic plasma jet in the experiment. The sensor in the pyrometer was a 256 pixel InGaAs array detector. The pyrometer had a total of 175 spectral wavelength channels with 4 nm wavelength intervals. The spectra were separated using Czerny-Turner dispersion gratings. The InGaAs detector measured the entire spectrum within a wavelength range of 1.0–1.65 μm in one fast scan. The irradiation was collimated by a spherical mirror. A plane grating then diffracted the collimated light with the resulting diffracted light focused by a second spherical mirror. Then, the image was projected onto the InGaAs detector array that recorded a fast scan of the spectrum. The spectral intensity response characteristics, the stray spectral light correction, and the temperature measurement accuracy for this pyrometer were investigated using a standard blackbody source in previous studies [31–33]. The measurement uncertainty was less than 5 °C in the temperature range of (500 °C, 1400 °C) for the blackbody measurements. The experimental system to measure the temperatures along the sharp leading edge in the plasma aerodynamic environment using the near-infrared multispectral pyrometer is shown in Fig. 2.

The supersonic plasma jet was produced by a high-power arc heater with the jet flowing through the test chamber [1–5]. A ceramic model of the leading edge was placed in the test chamber and exposed to the extreme convective heating from the high-enthalpy plasma flow with a total enthalpy of 2.0 MJ/kg and speeds of Mach 4-5. The model surface was painted with a high-absorption coating with a gray emissivity of 0.85. The leading edge cross section was a cylinder-wedge with a radius of 1.5 mm and a half angle of 6 deg as shown in Fig. 3. The entire model was 80 mm long and 80 mm high. A bow shock [3] formed in front of the leading edge as shown in Fig. 3(*a*). The shock region compressed the gases and increased the pressure, density, and temperature. The stagnation point was on the leading edge of the wing. The high-enthalpy gas in the bow shock impinged on the leading edge with the gas flow decelerated at the stagnation point to form a thin boundary layer and a local subsonic region. The surface temperature distribution depends on the complex energy balance at the surface. The heat transfer processes include the convective heating through the boundary layer, the radiation to and from the surface, the boundary layer, the interactions between the plasma jet and the environment, the conduction into the model interior, and the chemical reaction heating from exothermic recombination of atoms in the plasma at the surface. Thus, the surface temperature cannot be accurately predicted due to the complex heat transfer processes, complex flow field, environmental conditions, and material property variations at high temperatures. Therefore, experimental measurements of the surface temperatures are needed to evaluate the model designs in harsh aerodynamic environments.

The near-infrared multispectral pyrometer was aimed at a region near the leading edge on the surface of the experimental model through the quartz window in the test chamber. The effect of the quartz window on the measured spectral radiation intensities was calibrated by transmission measurements of the quartz window. The pyrometer measurement region was a 65 mm

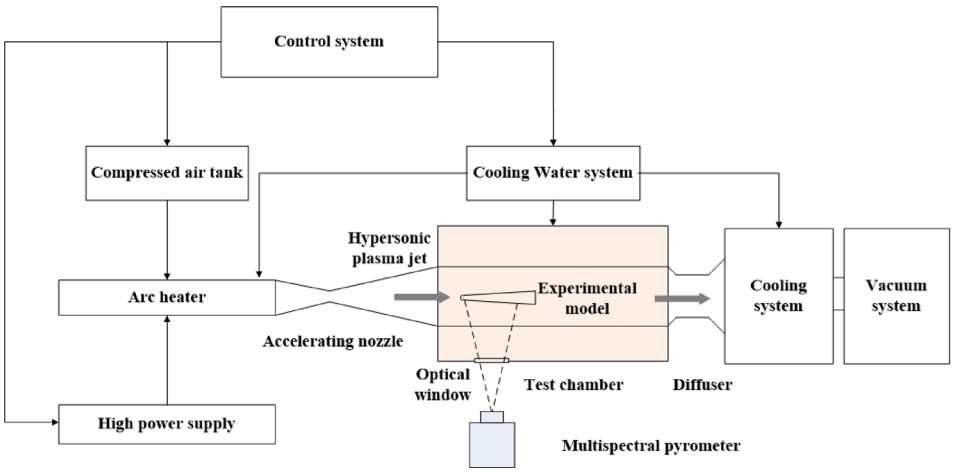

Fig. 2 Sketch of the experimental system to measure temperatures in plasma aerodynamic environments

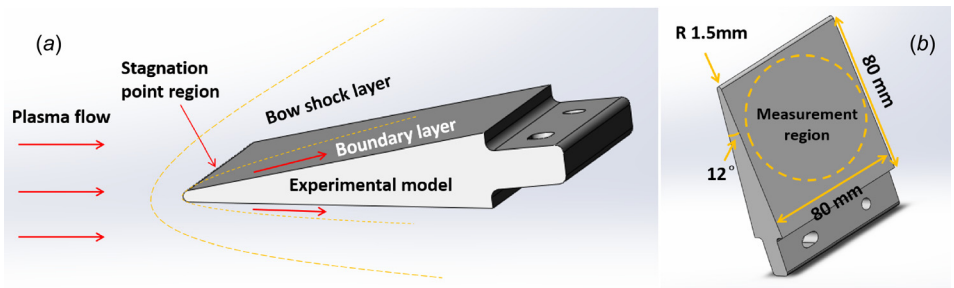

Fig. 3 Experimental model and the 65 mm diameter temperature measurement region

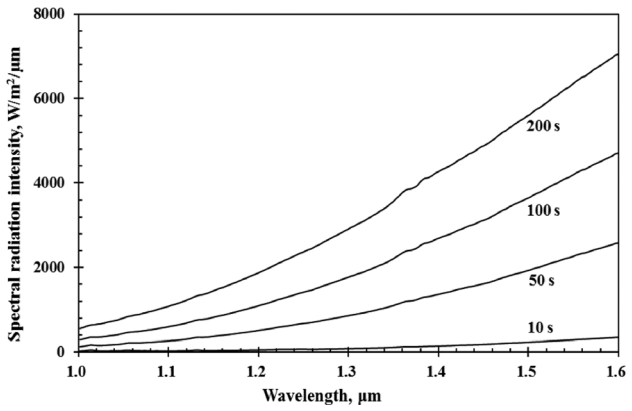

Fig. 4 Spectral radiation intensities in the measurement region for wavelengths of 1.0–1.6 μm at various times

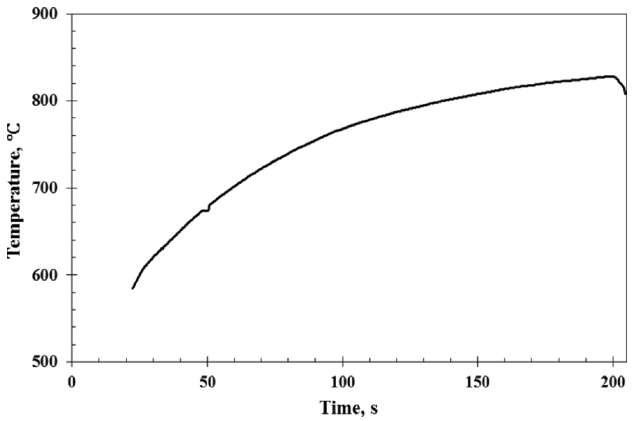

Fig. 5 Calculated weighted surface temperatures given by the traditional multispectral pyrometry measurement mode

diameter circle as shown in Fig. 3(*b*). The experiment lasted 200 s after the arc heater was started. The pyrometer recorded the near-infrared spectral intensities emitted from this region for wavelengths of 1.0–1.6 μm during the experiment. Figure 4 shows that the measured spectral radiation intensities at various wavelengths and times of 10 s, 50 s, 150 s, and 200 s. The spectral radiation intensity initially rapidly increased with time and was approaching steady-state.

In the traditional multispectral pyrometry measurement mode, this region would be assumed to be an isothermal "point." The average "point" temperature would then be calculated using the measured spectral intensities at multiple wavelengths based on Eq. (2) with the results shown in Fig. 5. The "point" temperature is the weighted temperature of the spatially averaged region which rapidly increased to 585 °C during the initial 20 s and then increased further to 828 °C with the aerodynamic heating. After the arc heater was shut down at 200 s, the temperature rapidly decreased. Although the temperature variations are consistent with the experimental conditions, the average "point" temperature results cannot be used to evaluate the large temperature gradients in the measurement region.

The temperature area fraction function, $r(T)$, describing the temperature nonuniformity in the measurement region for the field measurement mode was calculated using the improved Levenberg–Marquardt algorithm based on Eqs. (5)–(7). The penalty parameter was set to $\nu = 10^5$ [38]. The measurement uncertainty of the spectral radiation intensity by this pyrometer was assumed to be 1.0% based on the measurement noise. The

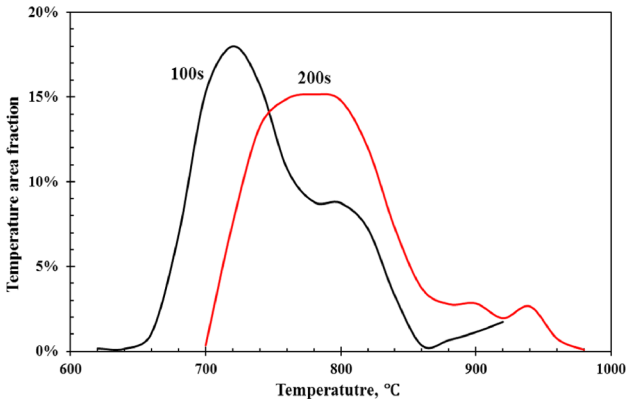

Fig. 6 Temperature area fraction distributions at 100 s and 200 s of the measurement region

temperatures were calculated using 1000 inverse calculations using the improved algorithm for various random noise levels with a normal distribution. The average results for the 1000 calculations were then used as the inverse solutions. Then, the temperature area fractions of the measurement region shown in Fig. 3(*b*) were determined at each time using the measured multispectral intensities. Figure 6 shows the calculated temperature area fractions at 100 s and 200 s as examples.

At 100 s with the weighted temperature of 768 °C as shown in Fig. 5, the actual calculated temperature range in the 65 mm diameter region ranged from 620 °C to 920 °C based on the multispectral pyrometer measurements operating in the field measurement mode. The temperature area fraction distributions were not the same at different temperatures as the temperature gradients changed significantly in the measurement region. The temperatures at 100 s were mainly ranged from 660 °C to 860 °C, while the sum of the temperature area fractions was about 96.2%. The largest temperature area fraction of 18% was at 720 °C. The temperature area fraction then decreases with increasing temperature to a minimum of 0.3% at 870 °C. The temperature area fraction then slightly increases at temperatures above 870 °C to a maximum of 1.7% at the maximum temperature of 920 °C.

At 200 s with the weighted temperature of 828 °C as shown in Fig. 5, the calculated temperatures in the measurement region are higher with temperatures from 700 °C to 980 °C. The temperature area fraction distribution at 200 s is similar to that at 100 s with the peak temperature area fraction of 15.2% moved to a higher temperature of 780 °C. The temperature distribution mainly ranges from 720 °C to 940 °C, and the sum of the temperature area fractions is about 98.8%. The temperature area fractions are higher at higher temperatures. In addition, the temperature area fraction distribution around the peak temperature is more uniform at 200 s than at 100 s. The temperature area fraction then becomes very small and is only 0.1% at the maximum temperature of 980 °C.

The subpixel temperature distributions were verified using a visible–infrared multispectral synchronous imaging pyrometer to simultaneously measure the two-dimensional temperature distribution of the ceramics model surface during the tests [13]. The temperature measurement uncertainty of this imaging pyrometer was within (0.21 °C, 0.99 °C) for temperatures of (600 °C, 1800 °C) for blackbody measurements [13]. The uncertainty was obtained assuming a relative signal measurement uncertainty of 1/250 and an ideal emissivity of 1.0 which represents the calibration precision of this pyrometer for standard experiments. This uncertainty will be larger for larger signal measurement uncertainties or larger emissivity uncertainties. The temperature uncertainty of the imaging pyrometer for these ceramic model measurements was evaluated based on a relative emissivity uncertainty of $\Delta\varepsilon/\varepsilon=10\%$ and the measured signal amplitudes [13]. Thus, the temperature uncertainty of this imaging pyrometer was within (9.7 °C, 13.6 °C) in this measurement region for the ceramic model surface.

The two-dimensional temperatures obtained by this calibrated imaging pyrometer were treated as the "true" temperature distribution on the model surface. This imaging pyrometer was slow with a maximum frame rate of 15 Hz at the full frame output, much slower than the high-speed point multispectral pyrometer. Figure 7 shows a measured thermal image (*a*) of the model surface at a high temperature with pseudo-color images of the two-dimensional temperature distribution at 100 s (*b*) and 200 s (*c*) measured by the imaging pyrometer. A significant temperature gradient was observed near the leading edge stagnation region facing the plasma jet. The maximum temperature is at the stagnation region after the shock wave on the upper leading edge of the model. The temperatures are higher, and the temperature increases are larger on the upper part of the leading edge of the model. The maximum temperature difference across the model surface was about 370 °C (629–999 °C) at 100 s and 438 °C (680–1118 °C) at 200 s.

The 65 mm diameter region in the field view of the multispectral pyrometer covers most of the model surface except near the stagnation region. The average temperatures of this point region measured by the two pyrometers are very close. For example, the average temperature at 100 s measured by the multispectral pyrometer operating in the field measurement mode based on Eq. (4) was 750 °C, while that measured by the imaging pyrometer was 751 °C, while that measured by the multispectral pyrometer at 200 s was 800 °C and that measured by the imaging pyrometer was 801 °C. The weighted average temperatures given by the traditional multispectral pyrometry at 100 s and 200 s were

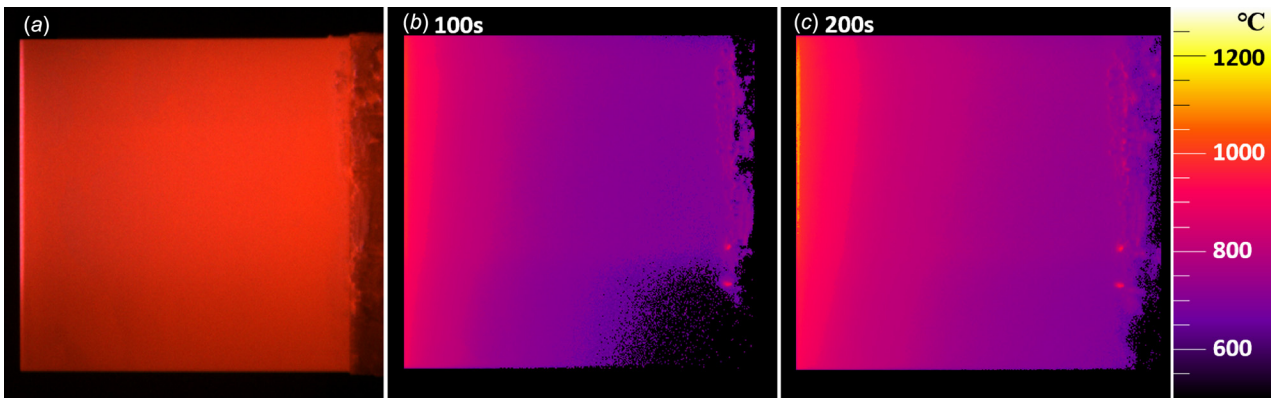

Fig. 7 Measured thermal image (*a*) of the model surface at high temperatures and pseudo-color results of temperature distributions on the model surface obtained by the imaging pyrometer at 100 s (*b*) and 200 s (*c*)

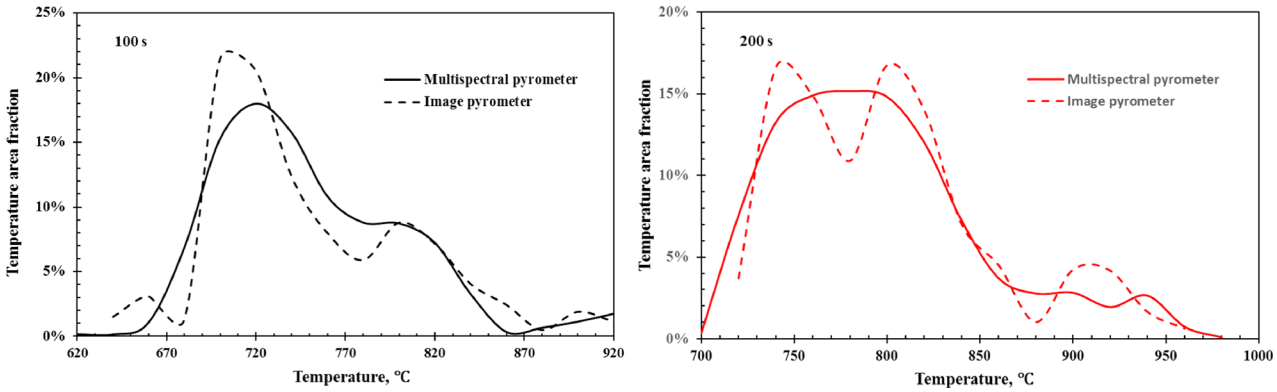

Fig. 8 Subpixel temperature area fraction distributions at 100 s and 200 s from the multispectral pyrometer and imaging pyrometer results

768 °C and 828 °C as shown in Fig. 5. Thus, the average temperature obtained by the multispectral pyrometer operating in the field measurement mode agrees better with the "true" value and is more representative than the average temperature measured by the traditional multispectral pyrometry.

The distributions of the temperature area fraction, $r(T)$, in the measurement region were calculated from the imaging pyrometer measurements using the same subpixel analysis as used in the multispectral pyrometer operating in the field mode based on the measured two-dimensional temperatures at the two heating times shown in Fig. 7. Figure 8 compares the subpixel temperature area fractions at heating times of 100 s and 200 s from the multispectral pyrometer and the imaging pyrometer. The calculated temperature ranges shown in Fig. 8 agree well except at low temperatures.

At 100 s, the temperature area fraction distributions are approximately the same for the two pyrometers. The imaging pyrometer peak is near 700 °C with a peak temperature area fraction of 21.5%, somewhat larger than the peak of 18.0% with the multispectral pyrometer. The sums of the temperature area fractions in the peak region of 680–760 °C are very close (63.6% for the imaging pyrometer and 66.7% for the multispectral pyrometer). The temperature area fraction distribution obtained by the multispectral pyrometer is smoother than that of the imaging pyrometer.

At 200 s, the imaging pyrometer distribution has two strong peaks at 740 °C and 800 °C. The peaks are both close to 16.6% and larger than the peak of 15.2% obtained by the multispectral pyrometer. There are large differences in the shapes of temperature area fraction distributions given by the two pyrometers. These differences mainly arise from the algorithm itself for this ill-posed inverse problem so further work is needed to improve the accuracy of this ill-posed inverse problem. Although the subpixel temperature distribution calculated from the multispectral pyrometer measurements in the field measurement mode are unable to discriminate the fine characteristics of the two peaks, the temperature area fraction sums are still similar. Between the peaks at 740 °C and 800 °C, the temperature area fraction sums are nearly the same for the imaging pyrometer (59.0%) and the multispectral pyrometer (58.1%).

Thus, the nonuniform temperature characteristics represented by the temperature area fractions from the multispectral pyrometer are quite accurate and agree well with the results from the imaging pyrometer measurements. The experimental results verify the applicability of the high speed multispectral pyrometer for measuring the temperature distribution near sharp leading edges and other objects with temperature gradients in supersonic plasma jet environments.

4 Conclusions

A high speed near-infrared (1.0–1.65 μm) multispectral pyrometer was used for in situ fast, noninvasive measurements of subpixel temperature distributions on high-temperature components exposed to supersonic plasma jets. Multispectral pyrometers generally make zero-dimensional measurements so they cannot measure surface temperature profiles on objects with temperature gradients like the leading edges of wings. However, a multispectral pyrometer can also be operated in the field measurement mode to measure temperature distributions. The measurements are based on a temperature area fraction that represents the subpixel temperature distribution information inside one pixel. Multiple spectra are then used to determine each temperature area in the measurement region. The spatial resolution of the multispectral pyrometer is then not restricted to one "pixel," but can be resolved into subpixel temperature distributions inside the point region. The method was illustrated by measurements on a ceramic model of a wing leading edge in a high-enthalpy plasma environment. The accuracy of the subpixel temperature distribution was verified by comparisons to simultaneous images from an imaging pyrometer for measurements of the two-dimensional temperature distribution on the model surface. The calculated average temperature and the temperature area fraction distribution at various heating times obtained from the multispectral pyrometer measurements agree well with those measured by the imaging pyrometer. The comparisons verify the ability of the high-speed multispectral pyrometer to measure the temperature distribution on objects in supersonic plasma jet environments.

Acknowledgment

We thank Professor D. M. Christopher for editing the English.

Funding Data

- National Key Research and Development Program of China (Grant No. 2016YFC0802500).
- National Natural Science Foundation of China (Grant No. 51576110).
- Opening Foundation of State Key Laboratory of High Temperature Gas Dynamics.
- Science Fund for Creative Research Groups (Grant No. 51621062).

References

[1] Monteverde, F., and Savino, R., 2007, "Stability of Ultra-High-Temperature ZrB2–SiC Ceramics Under Simulated Atmospheric Re-Entry Conditions," J. Eur. Ceram. Soc., **27**(16), pp. 4797–4805.
[2] Marschall, J., and Fletcher, D. G., 2010, "High-Enthalpy Test Environments, Flow Modeling and In Situ Diagnostics for Characterizing Ultra-High Temperature Ceramics," J. Eur. Ceram. Soc., **30**(11), pp. 2323–2336.
[3] Squire, T. H., and Marschall, J., 2010, "Material Property Requirements for Analysis and Design of UHTC Components in Hypersonic Applications," J. Eur. Ceram. Soc., **30**(11), pp. 2239–2251.
[4] Monteverde, F., Savino, R., Fumo, M., and Maso, A., 2010, "Plasma Wind Tunnel Testing of Ultra-High Temperature ZrB2–SiC Composites Under Hypersonic Re-Entry Conditions," J. Eur. Ceram. Soc., **30**(11), pp. 2313–2321.

[5] Cardone, G., 2007, "IR Heat Transfer Measurements in Hypersonic Plasma Flows," Quant. InfraRed Thermography J., **4**(2), pp. 233–251.
[6] Ranc, N., Pina, V., Sutter, G., and Philippon, S., 2004, "Temperature Measurement by Visible Pyrometry: Orthogonal Cutting Application," ASME J. Heat Transfer, **126**(6), pp. 931–936.
[7] Bendada, A., and Lamontagne, M., 2004, "A New Infrared Pyrometer for Polymer Temperature Measurement During Extrusion Moulding," Infrared Phys. Technol., **46**(1–2), pp. 11–15.
[8] Simmons, D. F., Fortgang, C. M., and Holtkamp, D. B., 2005, "Using Multispectral Imaging to Measure Temperature Profiles and Emissivity of Large Thermionic Dispenser Cathodes," Rev. Sci. Instrum., **76**(4), p. 044901.
[9] Mori, M., Novak, L., and Sekavčnik, M., 2007, "Measurements on Rotating Blades Using IR Thermography," Exp. Therm. Fluid Sci., **32**(2), pp. 387–396.
[10] Fu, T. R., Zhao, H., Zeng, J., Zhong, M. H., and Shi, C. L., 2010, "Two-Color Optical CCD-Based Pyrometer Using a Two-Peak Filter," Rev. Sci. Instrum., **81**(12), p. 124903.
[11] Fu, T. R., Zhao, H., Zeng, J., Wang, Z., Zhong, M. H., and Shi, C. L., 2010, "Improvements of Three-Color Optical CCD-Based Pyrometer System," Appl. Opt., **49**(31), pp. 5997–6005.
[12] Bai, H., Xie, Z., Zhang, Y., and Hu, Z., 2013, "Evaluation and Improvement in the Accuracy of a Charge-Coupled-Device-Based Pyrometer for Temperature Field Measurements of Continuous Casting Billets," Rev. Sci. Instrum., **84**(6), p. 064904.
[13] Fu, T. R., Liu, J. F., and Tian, J. B., 2017, "VIS-NIR Multispectral Synchronous Imaging Pyrometer for High-Temperature Measurements," Rev. Sci. Instrum., **88**(6), p. 064902.
[14] Vattulainen, J., Nummela, V., Hernberg, R., and Kytola, J., 2000, "A System for Quantitative Imaging Diagnostics and Its Application to Pyrometric In-Cylinder Flame-Temperature Measurements in Large Diesel Engines," Meas. Sci. Technol., **11**(2), pp. 103–119.
[15] Cignoli, F., De Iuliis, S., Manta, V., and Zizak, G., 2001, "Two-Dimensional Two-Wavelength Emission Technique for Soot Diagnostics," Appl. Opt., **40**(30), pp. 5370–5378.
[16] Payri, F., Pastor, J. V., García, J. M., and Pastor, J. M., 2007, "Contribution to the Application of Two-Colour Imaging to Diesel Combustion," Meas. Sci. Technol., **18**(8), pp. 2579–2598.
[17] Densmore, J. M., Biss, M. M., McNesby, K. L., and Homan, B. E., 2011, "High-Speed Digital Color Imaging Pyrometry," Appl. Opt., **50**(17), pp. 2659–2665.
[18] Yan, W., Zhou, H., Jiang, Z., Lou, C., Zhang, X., and Chen, D., 2013, "Experiments on Measurement of Temperature and Emissivity of Municipal Solid Waste (MSW) Combustion by Spectral Analysis and Image Processing in Visible Spectrum," Energy Fuels, **27**(11), pp. 6754–6762.
[19] Guo, H. Q., Castillo, J., and Sunderland, P., 2013, "Digital Camera Measurements of Soot Temperature and Soot Volume Fraction in Axisymmetric Flames," Appl. Opt., **52**(33), pp. 8040–8047.
[20] Kappagantula, K., Crane, C., and Pantoya, M., 2013, "Determination of the Spatial Temperature Distribution From Combustion Products: A Diagnostic Study," Rev. Sci. Instrum., **84**(10), p. 104902.
[21] Tapetado, A., Álvarez, J., Miguélez, H., and Vázquez, C., 2016, "Two-Color Pyrometer for Process Temperature Measurement During Machining, IEEE," J. Lightwave Technol., **34**(4), pp. 1380–1386.
[22] Tapetado, A., Álvarez, J., Miguélez, H., and Vázquez, C., 2017, "Fiber-Optic Pyrometer for Very Localized Temperature Measurements in a Turning Process," IEEE J. Sel. Top. Quantum Electron., **23**(2), p. 5601306.
[23] Ng, D., and Fralick, G., 2001, "Use of a Multiwavelength Pyrometer in Several Elevated Temperature Aerospace Applications," Rev. Sci. Instrum., **72**(2), pp. 1522–2530.
[24] Mazikowski, A., and Chrzanowski, K., 2003, "Non-Contact Multiband Method for Emissivity Measurement," Infrared Phys. Technol., **44**(2), pp. 91–99.
[25] Wen, C. D., and Mudawar, I., 2005, "Emissivity Characteristics of Polished Aluminum Alloy Surfaces and Assessment of Multispectral Radiation Thermometry (MRT) Emissivity Models," Int. J. Heat Mass Transfer, **48**(7), pp. 1316–1329.
[26] Sade, S., and Katzir, A., 2004, "Spectral Emissivity and Temperature Measurements of Selective Bodies Using Multiband Fiber-Optic Radiometry," J. Appl. Phys., **96**(6), pp. 3507–3513.
[27] Madura, H., Piatkowski, T., and Powiada, E., 2004, "Multispectral Precise Pyrometer for Measurement of Seawater Surface Temperature," Infrared Phys. Technol., **46**(1–2), pp. 69–73.
[28] Xiao, P., Dai, J. M., and Wang, Q. W., 2008, "Development of Multi-Target Multi-Spectral High-Speed Pyrometer," Spectrosc. Spectral Anal., **28**(11), pp. 2730–2734.
[29] Duvaut, T., 2008, "Comparison Between Multiwavelength Infrared and Visible Pyrometry: Application to Metals," Infrared Phys. Technol., **51**(4), pp. 292–299.
[30] Estevadeordal, J., Wang, G. H., Nirmalan, N., Wang, A. Q., Harper, S. P., and Rigney, J. D., 2013, "Multicolor Techniques for Identification and Filtering of Burst Signals in Jet Engine Pyrometers," ASME J. Turbomach., **136**(3), p. 031004.
[31] Fu, T. R., Wang, Z., and Cheng, X. F., 2010, "Temperature Measurements of Diesel Fuel Combustion With Multicolor Pyrometry," ASME J. Heat Transfer, **132**(5), p. 051602.
[32] Fu, T. R., Tan, P., Pang, C. H., Zhao, H., and Shen, Y., 2011, "Fast Fiber-Optic Multi-Wavelength Pyrometer," Rev. Sci. Instrum., **82**(6), p. 064902.
[33] Fu, T. R., Liu, J. F., Duan, M. H., and Zong, A. Z., 2014, "Temperature Measurements Using Multicolor Pyrometry in Thermal Radiation Heating Environments," Rev. Sci. Instrum., **85**(4), p. 044901.
[34] Fu, T. R., Liu, J. F., Tang, J. Q., Duan, M. H., Zhao, H., and Shi, C. L., 2014, "Temperature Measurements of High-Temperature Semi-Transparent Infrared Material Using Multi-Wavelength Pyrometry," Infrared Phys. Technol., **66**, pp. 49–55.
[35] Fu, T. R., Duan, M. H., Tian, J. B., and Shi, C. L., 2016, "Inverse Analysis of Non-Uniform Temperature Distributions Using Multispectral Pyrometry," Infrared Phys. Technol., **76**, pp. 504–509.
[36] Araújo, A., 2016, "Analysis of Multi-Band Pyrometry for Emissivity and Temperature Measurements of Gray Surfaces at Ambient Temperature," Infrared Phys. Technol., **76**, pp. 365–374.
[37] Daniel, K., Feng, C., and Gao, S., 2016, "Application of Multispectral Radiation Thermometry in Temperature Measurement of Thermal Barrier Coated Surfaces," Measurements, **92**, pp. 218–223.
[38] Burachik, R. S., and Kaya, C. Y., 2012, "An Augmented Penalty Function Method With Penalty Parameter Updates for Nonconvex Optimization," Nonlinear Anal., **75**(3), pp. 1158–1167.